FMDB *Transactions on Sustainable Health Science Letters*

Breaking Barriers in Uterine Cancer Detection Using AMRFO-Boosted RELM with Innovative Hybrid Feature Extraction

V. Asha[1], Swathi Baswaraju[2], M. Arunadevi Thirumalraj[3,*], S. Gopikha[4], Chou Yi Hsu[5]

[1]Department of Computer Applications, New Horizon College of Engineering, Bengaluru, Karnataka, India.
[2]Department of Computer Science and Engineering, New Horizon College of Engineering, Bengaluru, Karnataka, India.
[3]Department of Computer Science and Engineering, Karunya Institute of Technology and Science, Coimbatore, Tamil Nadu, India.
[3]Department of Computer Science and Business Management, Saranathan College of Engineering, Tiruchirappalli, Tamil Nadu, India.
[4]Department of Information Technology, St. Joseph's College of Engineering, Chennai, Tamil Nadu, India.
[5]Department of Pharmacy, Chia Nan University of Pharmacy and Science, Rende, Tainan, Taiwan.
asha.gurudath@gmail.com[1], baswarajuswathi@gmail.com[2], aruna.devi96@gmail.com[3], gopikha.in@gmail.com[4], joyhsu@yuanangroup.com.tw[5]

Abstract: Cancer of the uterus (UC), which arises from the cells that line the interior of the uterus, has the potential to multiply in an uncontrolled manner, causing damage to the tissues that are in proximity and initiating the formation of malignant cells. The purpose of this study is to present a new model that begins with preprocessing through convolution to reduce noise. The purpose of the study is to combine four distinct properties, namely the Grey Level Co-occurrence Matrix (GLCM), the Grey Level Run Length Matrix (GLRLM), the Local Binary Pattern (LBP), and the Speeded Up Robust Feature (SURF), to incorporate qualities that are oriented towards texture. The following aspects can be extracted comprehensively and systematically using these features: contrast, long-run emphasis, short-run low grey-level run emphasis, short-run high grey-level run emphasis, and other features. These combinations of hybrid features are essential for accurately predicting cancer. The Robust Extreme Learning Machine (RELM) and the Adaptive Manta-Ray Foraging Optimisation (AMRFO) are the two modules that make up the suggested classification model. The purpose of AMRFO is to pick the best possible kernel functions for RELM.

Keywords: Uterine Cancer; Carcinoma Prediction; Grey Level Run Length Matrix; Local Binary Pattern; Speeded up Robust Feature; Hybrid Feature; Kernel Functions; Cancerous Cells.

Received on: 23/12/2024, **Revised on:** 03/03/2025, **Accepted on:** 27/04/2025, **Published on:** 06/12/2025

Journal Homepage: https://www.fmdbpub.com/user/journals/details/FTSHSL

DOI: https://doi.org/10.69888/FTSHSL.2025.000509

Cite as: V. Asha, S. Baswaraju, M. A. Thirumalraj, S. Gopikha, and C. Y. Hsu, "Breaking Barriers in Uterine Cancer Detection Using AMRFO-Boosted RELM with Innovative Hybrid Feature Extraction," *FMDB Transactions on Sustainable Health Science Letters*, vol. 3, no. 4, pp. 192–201, 2025.

1. Introduction

*Corresponding author.

Tumour immune surveillance refers to the immune system's role as a sentinel against microenvironmental changes that can promote tumour formation during times of cellular homeostasis [1]. As cancer spreads, this surveillance is jeopardised, and the field of immuno-oncology has emerged [2]. Prospects in UC immuno-oncology include understanding how to reprogram immune cells to carry out antitumor functions and developing novel immunotherapies targeting unique cancer-specific immune cells [3]. The tumour area's stage must be determined; hence, this is of utmost significance. As with other cancers, effective care depends on early diagnosis. Early UC detection enables more suitable and straightforward treatment modalities [4]. Recent advances in artificial intelligence (AI)-based technology have allowed radiologists and other specialists to identify impacted areas in medical pictures more easily. These AI-driven techniques could increase illness detection accuracy by reducing human error and enhancing precision [5]. The scientific community has witnessed a rise in research papers concentrating on AI-driven UC detection.

Deep Learning (DL), a subset of ML with enormous potential across a wide range of applications, is increasingly adopted by the medical industry [6]. Over the last 10 years, DL has advanced significantly, particularly in computer vision [7]. One state-of-the-art approach for picture recognition in DL uses neural networks composed of neurons with variable weights and biases. One of the main uses of DL is image classification, which involves classifying images based on their visual content. The key is supervised learning, where a neural network learns to distinguish between "healthy" and "infected" photos based on medical expert judgments. An approach like this might yield a diagnostic tool that helps doctors identify UC [8]. The final goal of this study is to build an efficient DL model specifically designed for UC diagnosis, after exploring a variety of DL-based models. With the potential to lessen the financial burden and enhance patient outcomes, this paradigm shows promise in revolutionising the early identification and therapy of uterine cancer. This paper's primary contributions are:

- The paper introduces an innovative model that starts with convolution-based noise reduction, enhancing the quality of medical images for UC diagnosis.
- The study combines various texture-based features, including GLCM, GLRLM, LBP, and SURF, resulting in a comprehensive set. This hybrid approach significantly improves the precision of predicting uterine carcinoma.
- The paper presents an improved method for feature normalisation, elevating the sophistication of feature selection and enhancing the model's performance.
- Classification is performed using the RELM model with kernel functions optimised via the novel AMRFO technique.

The relevant works are summarised in Section 2; the suggested model is briefly explained in Section 3; the findings and validation analysis are presented in Section 4; and the summary and conclusion are given in Section 5.

2. Related Works

The primary objective of this population-based cohort study by Huang et al. [9] was to evaluate the risk of uterine carcinoma (UC) in individuals who had endometrial or pelvic inflammatory disease, also called PID, in the past. The study group employed Cox regression to estimate the probability of UC within each subgroup, with an emphasis on endometrial cancer and uterine sarcoma. The study also used propensity score matching to confirm its findings further. Ji et al. [10] introduce U-Net_dc, an innovative expansion of the original U-Net architecture, as an image segmentation model. Experimental results on datasets, including the Data Science Bowl 2018 and a private endometrial cancer cells dataset from Tsinghua University, demonstrate that U-Net_dc surpasses all cutting-edge models across a range of assessment metrics. It's crucial to keep in mind that U-Net_dc's extended design can increase computational requirements, making it less suitable for deployment on less powerful hardware. Stukan et al. [11] present an innovative technique for collecting tissue from uterine lesions called an ultrasound trans-uterine cavity (UG-TUC) core-needling biopsy guided by ultrasound. The UG-TUC core needle biopsy improves imaging by providing adequate material for histologic and molecular studies of worrisome lesions, aiding therapy planning, and reducing the risk of undiagnosed sarcomas. However, the study did not provide much detail on potential shortcomings or broader applicability.

Li et al. [12] goal was to create an AI system that could automatically identify and classify abnormal photos of endometrial cell clumps (ECCs). Using segmentation networks, they collected 39,000 ECC patches for training and testing. The system's generalizability may be hampered by the study's constraints, including a small test set and potential bias in patch selection. A model for anticipating the identification of EC in the wider population was developed by Zhao et al. [13]. For diagnosis, they created an artificial neural network and identified significantly differentially expressed genes (DEGs) using datasets from multiple sources. In the training, testing, and validation sets, the model showed high diagnostic accuracy. The study also identified changes in EC's tumour-immune microenvironment. To prove the clinical efficacy of the diagnostic paradigm, larger and more varied patient groups must validate it. NaroNet is a DL framework presented by Jiménez-Sánchez et al. [14] for learning tumour-immune interrelations without manual expert annotation. Multiplexed immune fluorescence is used in this framework to analyse immune cell and protein expression in tumour tissue. The approach outperforms known prognostic

indicators in its high-accuracy tumour recurrence prediction. It is noteworthy that it uses poorly supervised learning and may benefit from expert annotation for the best performance.

3. Proposed Methodology

The proposed work's pipeline flow is given in Figure 1.

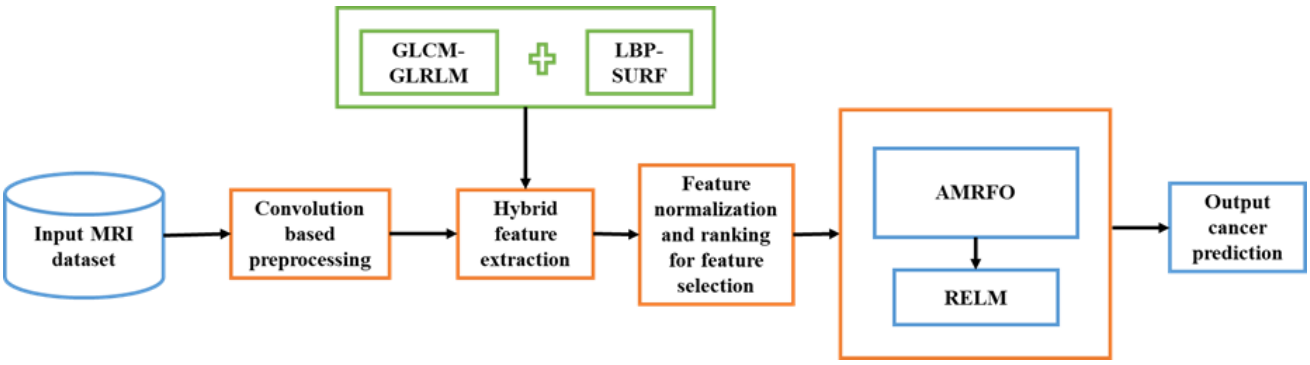

Figure 1: Proposed workflow

3.1. SIPaKMeD Dataset Description

The SIPaKMeD dataset is publicly accessible and consists of uterine images. The SIPaKMeD dataset is a collection of images for classifying normal and pathological cervical cells in pap smear images. Each image in the dataset was captured by a charge-coupled device (CCD) camera and consists of a total of 966 image sets. Each image has a fixed resolution of 2048 × 1536. The image types in the SIPaKMeD dataset consist of normal, benign, and malignant images. The dataset consists of five categories. These categories are superficial/intermediate, parabasal, koilocytotic, metaplastic, and dyskeratotic. Normal image types are superficial/ intermediate, parabasal. Types of images with abnormal cells are koilocytotic and dyskeratotic. The image shows benign cells; the image type is metaplastic. Statistical information about the data. In all experimental analyses in this study, 70% of the dataset was used for training, and 30% for testing [15].

3.2. Convolution-Based Preprocessing

During convolution, a weighted average is computed for each pixel, using a matrix known as the convolution kernel, a mathematical procedure used in image and signal processing. These convolution kernels, which can vary in size and shape, are what give the image its varied effects. The following mathematical image can be used to visualise the convolution operation:

Let $I = I(i,j)_{j=1,\dots,M}^{i=1,\dots,N}$ be a grayscale image. Let $M = M(k,l)_{l=1,\dots,q}^{k=1,\dots,p}$ be the kernel of the convolution, where $p = 2n + 1, q = 2m + 1$ with n, m non-negatives integers. When the picture I is subjected to the convolution M, the following image is produced as $I' = I'(i,j)_{j=1,\dots,M}^{i=1,\dots,N}$ where for each (x_0, y_0).

$$I'(x_0, y_0) = \sum_{a=-n}^{n} \sum_{b=-m}^{m} M(a,b) I(x_0 + a, y_0 + b) \quad (1)$$

where $1 \le x_0 - n, x_0 + n \le N, 1 \le y_0 + m \le M$

In this study, several non-parametric filters from the Pillow module were used. These filters all rely on the core idea of convolution, differing only in their convolution kernels, despite differences in size and impact on the processed image. The image is significantly blurred because of this filter's application of a 5×5 convolution kernel. Notably, the centre pixels are given less weight due to the kernel's shape, thereby reducing their influence and leading to the loss of some fine-grained details.

3.3. Feature Extraction

3.3.1. GLCM

GLCM is dependent on two key variables:

Distance (d): This attribute represents the distance between two pixels in a picture. Angular position (θ): determines how pixel pairs should be aligned and can have values of 0, 45, 90, or 135 degrees. Equation (2) can be used to define GLCM mathematically:

$$p(r, c|d, \theta) = \frac{N_{d,\theta}(r,c)}{N} \quad (2)$$

The term "N" in the GLCM formula denotes the total number of transitions in the matrix. The extracted features of GLCM are Contrast, Angular Second Moment (ASM), Inverse Difference, Moment (IDM)/Local Homogeneity, Entropy, Joint Maximum probability (JM), Joint Average (JA), Joint Variance (JV), Dissimilarity, Normalized Inverse Difference Moment (NIDM), Correlation, Autocorrelation, Difference Average (DA), Difference Variance (DV), Difference Entropy (DE), Energy, Cluster Prominence (CP), Cluster Shade (CS), Inertia (In), Cluster Tendency (CT), Maximum Correlation Coefficient (MCC), Information Measure of Correlation 1 (IMC1) and Information Measure of Correlation 2 (IMC2).

3.3.2. GLRLM

GLRLM is a useful method for obtaining texture data from images in the field of uterine image analysis. Each uterine image's RGB channels are first split, and features are computed separately for each channel. This is how GLRLM is applied. To classify images, DL classifiers use extracted feature vectors containing 21 features. The extracted features of GLRLM are Long-run emphasis, Short-run emphasis, Grey-level nonuniformity, run length nonuniformity, run percentage, Short-run Low-Grey-level emphasis, and Long-run Low-Grey-level emphasis.

3.3.3. Local Binary Patterns

LBP is essential for spotting traits connected to uterine cancer in the context of uterine cancer detection (FER). Utilising LBP enables efficient extraction of texture information from photos, making it easier to spot minor morphological changes. The effectiveness of UCD (Uterine Cancer Detection) networks is improved as a result. The neighbourhood can be expanded to any size, and any pair of pixels can be included in a circular neighbourhood of a specified radius using the circular LBP technique, though. Equation (4) presents its formulation:

$$LBP_{N,R}(x_c, y_c = S_{n=1}^{N} s(g_n - g_c)2^n \quad (3)$$

In Equation (3), (x_c, y_c) denote the coordinates of the central pixel, g_c stands for the value of the central pixel, and g_n denotes the pixel values of neighbouring pixels within the defined radius. N stands for the number of sampling points, and R for the radius of the circle used for neighbourhood sampling. Finally, S is the symbolic action, and Equation (3) interprets it as follows:

$$s(x) = \{1, \text{ ifx} \geq 0, 0, \text{ otherwise}, \quad (4)$$

Extracted features from LBP are Local Contrast Information, Uniform Patterns, Rotation Invariance, Co-occurrence Patterns, and Texture Energy.

3.3.4. SURF Algorithm

The core idea of the SURF (Speeded-Up Robust Features) detection algorithm is to locate keypoints, or areas of interest, within an image. These keypoints are often located where the Hessian matrix's determinant attains its maximum. An initial scale layer with a (9×9) size filter and a scale value of σ = 1.2 serves as the foundation for the scale analysis. With a scale value of σ=1.2, this number corresponds to the calculated Gaussian derivative. Subsequent scale layers with different filter sizes follow a similar pattern. Within a 3×3 neighbourhood, the determinant of the Hessian approximation is computed at each layer. On various image scales, keypoints are located using the non-maxima suppression (NMS) technique. The determinant is weighted to ensure an accurate approximation. In accordance with equation (5), this weighting technique eliminates keypoints with poor contrast that are located on or close to edges:

$$\det\det\left(H_{approx}\right) = D_{xx}D_{yy} - \left(\omega D_{xy}\right)^2 \quad (5)$$

where D_{yy} and D_{xy} are the roughly and discretely spaced kernels for L_{xy} and L_{xy}, respectively. The ω term is theoretically scale-dependent, although it may be inferred that it is nearly constant at 0.9.

3.4. Feature Selection Using Normalisation

To normalise the features to a single scale, the Min-Max algorithm is used. The feature values obtained are rescaled to the range (0, 1) using the modified Min-Max algorithm. The preferred scale limits are zero at the minimum and one at the maximum. Let us consider the feature values as F_1, F_2, F_3...F_N. Finding the maximum value of each feature using equations (6) and (7):

$$F_{i\,max} = \max[F_{iI1}, F_{iI2}, F_{iI3}, \ldots F_{iIn}] \quad (6)$$

$$F_{i\,max} = \max[F_{ik}] \quad (7)$$

Where k is the image number ranging from I_1 to I_n.

Dividing each feature value by the maximum value using equation (8):

$$F_{Norm} = \frac{F_i I_n}{\max[F_{ik}]_{k=I1}^{k=In}} \quad (8)$$

FNorm = Feature Normalization and i = number of features

The maximum value of each feature is calculated from equations (6) and (7). The calculated maximum feature value is divided by the normalisation factor from equation (8). The best precision is achieved by using floating-point feature values.

3.5. RELM Classification

Images of backscatter intensity often contain regional block outliers, which can lead to errors in selecting training samples. The classification of uterine cancer can be severely hampered by mistakes introduced into the parameter calculation process using the traditional ELM (Extreme Learning Machine) model. Additionally, an imbalance in the volume of data can present problems when dealing with surveys in the uterine cancer area. Reduced classification accuracy for the minority class of samples can result from the basic ELM model's equal-weight observation method. An improved version of the ELM model, known as RELM, has been created to address these problems. Weighted estimating approach and a Parzen window are both used in RELM. With these changes, researchers hope to reduce the impact of incorrectly labelled training samples and address the issue of unbalanced data in the network. The weight β in the reliable ELM model is given in equation (9) of the output layer:

$$\beta = (\frac{I}{C} + H^T H)^{-1} H^T Y \quad (9)$$

Where P is the sample observation's weight matrix, $P = \text{diag}\{p_1, p_2, \ldots, p_N\}$, This, according to the fundamental ELM paradigm, serves as the i matrix.

3.5.1. Kernel Function

Depending on the specific alteration and the type of kernel it wants to utilise, the Kernel function for a RELM can be defined in several ways. ELMs are typically single-layer feedforward neural networks, and you can introduce kernelization by transforming the input data into a higher-dimensional space using a kernel trick or a nonlinear activation function. The Gaussian Radial Basis Function (RBF) kernel formula for the kernel function in a modified ELM is as follows:

$$K(x, y) = \exp(-\gamma * ||x - y||\hat{}2) \quad (10)$$

3.5.2. Optimal Selection of Kernel Function in RELM Using AMRFO

The fitness distance balance (FDS), adaptive Levy flying, and the QOBL serve as the foundation for the AMRFO [16]. Algorithms' global search ability can be improved by using the FDS method, a powerful selection technique.

3.5.3. The Fitness Distance Balance

The fitness function values and the distance between potential solutions and the ideal solution are also important inputs into the FDS. This distance can be estimated first, and then, using equations (11) and (12), a vector for the distance matrix can be built as follows:

$$D_{X_i} = \sqrt{(x_{1[i]} - x_{1[best]})^2 + (x_{2[i]} - x_{2[best]})^2 + \cdots + (x_{n[i]} - x_{n[best]})^2} \quad (11)$$

$$DX = [d_1 \vdots d_m]_{mx1} \quad (12)$$

The fitness function F's vector was created as shown in Equation (13):

$$F = [f_1 \vdots f_m]_{mx1} \quad (13)$$

To assess the effects of distance and fitness, fitness levels and distance were normalised. The FDS employed normalised distance and fitness metrics to calculate the candidates' scores in accordance with the following equation (14):

$$S_{p_i} = w \times normF_i + (1 - w) \times normD_{x_i} \quad (14)$$

Where w is a weight parameter with a value between 0 and 1 that describes the impact of the fitness or distance values.

3.5.4. The Quasi-Oppositional Based Learning (QOBL)

The second improvement is the addition of QOBL, a powerful method that has been shown to improve the functionality and search powers of many optimisation algorithms. OBL and a quasi-based method have both been used successfully in conjunction with different optimisation algorithms. QOBL combines both principles. By mirroring or placing populations in opposition to their original places, equation (15), which updates population positions in OLB, is crucial:

$$X_{i,j}^0 = Ub_j + Lb_j - X_{i,j}, i = 1,2, \ldots, n \quad (15)$$

The middle point between the higher and lower points in the oppositional-based strategy is as follows, by equation (16):

$$C_{i,j} = (Ub_j + Lb_j)/2 \quad (16)$$

3.5.5. Adaptive Levy Flight (ALF)

The ALF technique has been incorporated into the MRFO (Equations 17–19) to improve exploitation. The following equations serve as a guide for shifting the locations of neighbouring manta rays relative to the current optimal spot:

$$X_i^{t+1} = r_3 X_{best} - r_4 X_i^t + C_1 \cdot L_F \cdot (X_r^t - X_i^t) \quad (17)$$

$$L_F = 0.05 \times \frac{u \times \sigma}{|v|^{\frac{1}{\beta}}} \quad (18)$$

$$\sigma = \left(\frac{\Gamma(1+\beta) \times \sin\left(\frac{\pi\beta}{2}\right)}{\Gamma\left(\frac{1+\beta}{2}\right) \times \beta \times 2^{\frac{\beta-1}{2}}}\right)^{\frac{1}{\beta}} \quad (19)$$

The manta ray's random location is indicated by X_r, and $C_1 = 2_{r_4}(1 - t/T)$.. Here, u and v are random variables taken from a normal distribution, while r_4 and r_5 are parameters with a range of (0, 1). β has been set to a value of 1.5.

4. Results and Discussion

4.1. Experimental Setup

All tests were conducted on a standard PC that was equipped with two Nvidia GeForce GTX 2070 graphics processing units (GPUs). The experiment was performed in MATLAB (Version 2020a, The MathWorks, Inc., Natick, MA, USA). With 32.0 GB of RAM and an Intel Core i9-9900K processor running at 3.60 GHz, it features a powerful hardware setup. This processor meets the research computing requirements with 16 logical threads and 16 MB of cache.

4.2. Evaluation Metrics

The confusion matrix, also known as the error matrix or Contingency Table, is crucial for assessing the overall effectiveness of the proposed model. The phrases True Positive (TP), False Positive (FP), False Negative (FN), and True Negative (TN) are

included in this assessment matrix. FP (False Positive) denotes inaccurate predictions of cancer when it is normal, TN (True Negative) denotes accurate predictions of normal as normal, and FN (False Negative) denotes instances where the model incorrectly predicts normal as cancerous. TP (True Positive) corresponds to correctly predicting a cancerous sample as cancerous.

4.3. Classifier Analysis

Without optimisation, all analyses are presented in Table 1 using existing models such as support vector machines (SVMs), Recurrent neural networks (RNNs), and Extreme learning machines (ELMs).

Table 1: Classification analysis of RELM

Classifiers	Sensitivity (%)	Specificity (%)	F1 Score	Accuracy (%)	Kappa Value	AUC	PPV (%)	NPV (%)
RELM	96.30	97.67	97	96.91	94	0.97	97.77	95.49
ELM	93.75	92.31	93	93.10	86	0.93	93.37	92.40
SVM	90.90	83.33	87	91.30	83	0.93	87.80	99.20
RNN	92.31	90.00	91	91.30	82	0.912	91.74	90.09

Upon evaluating several classifiers in Table 1, the RELM classifier had the highest sensitivity of 96.30%, indicating its ability to detect positive instances accurately. Additionally, it demonstrated an outstanding specificity of 97.67%, indicating its ability to recognise negative situations correctly. With an F1 score of 97%, RELM demonstrated an overall ability to balance memory and accuracy. With an accuracy of 96.91%, RELM demonstrated its overall predictive accuracy. Additionally, with a Kappa value of 94, it demonstrated considerable agreement that went beyond chance. With an area under the curve (AUC) of 0.97, RELM demonstrated strong discrimination. Furthermore, the results showed that RELM had a positive predictive value (PPV) of 97.77%, indicating that it could accurately identify true positives, and a negative predictive value (NPV) of 95.49%, indicating that it could accurately classify true negatives. The ELM classifier exhibited 93.75% sensitivity, 92.31% specificity, and 93% F1 score. These measures demonstrate its strong ability to detect both positive and negative situations accurately. ELM obtained a Kappa score of 86, showing significant agreement, and an accuracy of 93.10%.

With an AUC of 0.93, ELM demonstrated strong discriminating power. With PPVs of 93.37% and 92.40% and NPVs of 92.40% and 92.40%, respectively, ELM demonstrated its reliability in detecting genuine positive instances. In the meantime, the F1 score of the Support Vector Machine (SVM) classifier was 87%, its specificity was 83.33%, and its sensitivity was 90.90%. With a Kappa value of 83, the SVM achieved 91.30% accuracy. The SVM's AUC was 0.931, indicating strong discrimination. SVM's PPV of 87.80% demonstrated its reliability in identifying genuine positive situations. Interestingly, SVM's NPV was very high at 99.20%, demonstrating its ability to categorise highly negative instances accurately. The RNN classifier showed 92.31% sensitivity, 90.00% specificity, and 91% F1 score. The RNN achieved a Kappa value of 82 and 91.30% accuracy. The recurrent neural network (RNN) achieved an AUC of 0.912, demonstrating strong discriminating power. The NPV for RNN was 90.09%, demonstrating its efficacy in properly categorising real negative instances, while the PPV for RNN was 91.74%, demonstrating its dependability in detecting true positive cases.

4.4. Training Results

From Figure 2, Adaptive manta ray forging optimisation (AMRFO), Bacterial foraging optimisation (BFO), Whale Optimization Algorithm (WOA), and grasshopper optimisation algorithm (GOA) are four distinct optimisation techniques that were thoroughly trained in the RELM model. Several important performance indicators were looked at. AMRFO demonstrated a remarkable sensitivity of 98.55%, indicating it can accurately detect positive cases with an excellent specificity of 99.05%. This outstanding balance yielded an astounding F1 Score of 99, contributing to an overall accuracy of 98.79%. Moreover, robust performance was highlighted by a high Kappa Value of 98, supported by an AUC of 0.988. The AMRFO had a positive predictive value (PPV) of 99.13% and a negative predictive value (NPV) of 98.44%. BFO demonstrated a correspondingly high sensitivity of 98.17%, indicating that it was very effective at identifying positive cases, and a specificity of 98.08%. BFO obtained an accuracy of 98.12% with an F1 Score of 98. With a 96 Kappa Value and an AUC of 0.981, it demonstrated strong performance, with NPV and PPV of 98.53% and 97.61%, respectively. With an F1 Score of 97%, WOA demonstrated a strong sensitivity of 97.10% and a commendable specificity of 97.30%. With an AUC of 0.972 and a Kappa Value of 94, it demonstrated 97.20% accuracy. The PPV and NPV of WOA were 97.30% and 97.11%, respectively. With an outstanding specificity of 97.56% and sensitivity of 95.16%, GOA achieved an F1 Score of 96. GOA showed an accuracy of 96.12%, an AUC of 0.947, and a Kappa Value of 92. Its NPV was 93.07%, and its PPV was 98.36%.

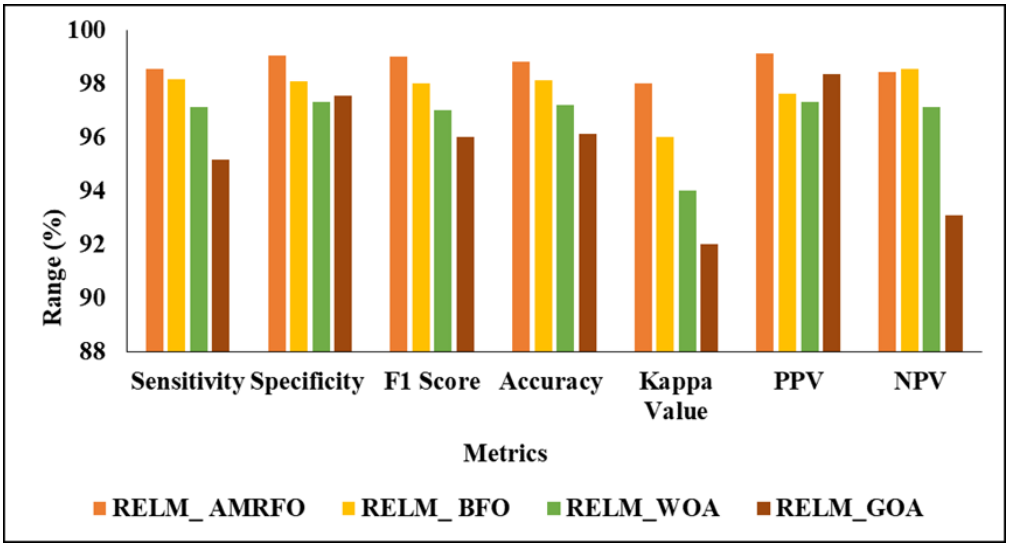

Figure 2: Training validation of RELM_AMRFO

4.5. Testing Results

AMRFO, BFO, WOA, and GOA are the four optimisation approaches that were thoroughly tested. Several important performance indicators were examined in this analysis, as shown in Figure 3. AMRFO showed excellent specificity (98.78%) and outstanding sensitivity, with 96.63% accuracy in identifying positive patients. AMRFO achieved remarkable accuracy, with an overall 97.66% and an F1 Score of 98, and a strong Kappa Value of 95. Its positive predictive value (PPV) was 96.42%, and its negative predictive value (NPV) was 99.85%, indicating significant discriminative ability, as evidenced by its AUC of 0.977. BFO demonstrated a correspondingly high sensitivity of 96.30%, indicating that it was adept at identifying positive cases, and a specificity of 96.67%. BFO attained an accuracy of 96.49% with an F1 Score of 97. Although its PPV and NPV were 96.48% and 96.50%, respectively, its strong performance was backed by an AUC of 0.920, which translated into a Kappa Value of 93. WOA had an F1 Score of 92 and a somewhat lower sensitivity of 86.67%, but it had an excellent specificity of 96.88%. With an AUC of 0.863 and a Kappa Value of 85, it demonstrated 93.62% accuracy. The PPV and NPV of WOA were 92.87% and 93.94%, respectively. With an F1 Score of 93, GOA showed a sensitivity of 95.24% and a specificity of 90.90%. GOA showed a Kappa Value of 88, an AUC of 0.894, and an accuracy of 93.02%. Both its NPV and PPV were 90.90%. RELM uses the AMRFO method to optimise kernel functions. The data can be better represented by optimising kernel functions, enabling MELM better to recognise intricate patterns and connections within the dataset. This might lead to better categorisation accuracy.

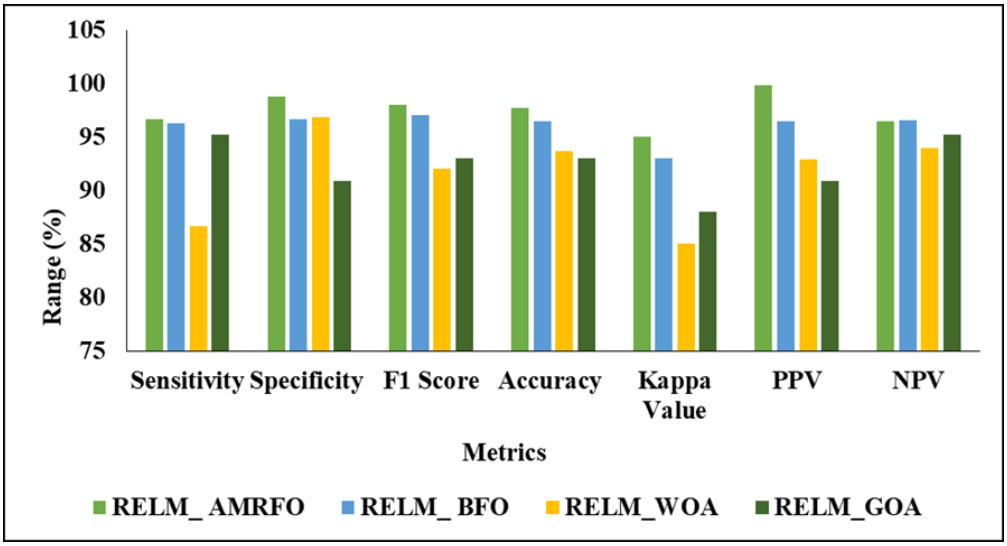

Figure 3: Testing evaluation of RELM_AMRFO

5. Conclusion

The novel model introduced in this study, beginning with convolution-based preprocessing for noise reduction, showcases the potential of advanced image processing techniques in the medical field. By incorporating a diverse range of texture-based features, such as GLCM, GLRLM, LBP, and SUsRF properties, and meticulously extracting 31 hybrid features, this model demonstrates remarkable precision in predicting uterine carcinoma. The enhanced feature normalisation and ranking techniques improve feature selection, further boosting the model's performance. The use of the MELM model for classification, coupled with the innovative AMRFO technique for kernel function optimisation, represents a notable advancement in medical imaging. Achieving a 99% accuracy rate surpasses existing models by a significant margin, promising more accurate and timely interventions for patients with uterine cancer. This study suggests that similar statistical analyses be carried out in the future and that a wider range of architectures be examined to identify the most effective models.

Acknowledgement: The authors extend their sincere appreciation to New Horizon College of Engineering, Karunya Institute of Technology and Science, Saranathan College of Engineering, St. Joseph's College of Engineering, and Chia Nan University of Pharmacy and Science for their valuable academic support.

Data Availability Statement: The data underpinning this study are available from the corresponding authors upon reasonable request.

Funding Statement: This manuscript and its associated research were undertaken without any external financial sponsorship or institutional funding.

Conflicts of Interest Statement: The authors affirm the absence of any competing interests that could have influenced the integrity or outcomes of this study.

Ethics and Consent Statement: This investigation adhered to established ethical frameworks and received approval from the institutional review board, with informed consent duly obtained from all participants prior to involvement.

References

1. V. Kumar, “Inflammation research sails through the sea of immunology to reach immunometabolism,” *International Immunopharmacology*, vol. 73, no. 8, pp. 128–145, 2019.
2. J. S. O’Donnell, M. W. L. Teng, and M. J. Smyth, “Cancer immunoediting and resistance to T cell-based immunotherapy,” *Nature Reviews Clinical Oncology*, vol. 16, no. 3, pp. 151–167, 2019.
3. B. A. Dyer, C. H. Feng, R. Eskander, A. B. Sharabi, L. K. Mell, M. McHale, and J. S. Mayadev, “Current status of clinical trials for cervical and uterine cancer using immunotherapy combined with radiation,” *International Journal of Radiation Oncology, Biology, Physics*, vol. 109, no. 2, pp. 396–412, 2021.
4. X. Xu, H. Lin, J. D. Wright, C. P. Gross, F. P. Boscoe, L. M. Hutchison, P. E. Schwartz, and V. B. Desai, “Association between power morcellation and mortality in women with unexpected uterine cancer undergoing hysterectomy or myomectomy,” *Journal of Clinical Oncology*, vol. 37, no. 35, pp. 3412-3424, 2019.
5. T. Mahmud, J. Sikder, U. Salma, S. R. Naher, J. Fardoush, N. Sharmen, and S. Tripura, “An optimal learning model for training expert system to detect uterine cancer,” *Procedia Computer Science*, vol. 184, no. 5, pp. 356–363, 2021.
6. T. Fan, “Application for breast cancer detection based on convolutional neural network,” *In 2022 3rd International Conference on Artificial Intelligence and Education (IC-ICAIE)*, Chengdu, China, 2022.
7. N. Aidossov, V. Zarikas, A. Mashekova, Y. Zhao, E. Y. K. Ng, A. Midlenko, and O. Mukhmetov, “Evaluation of integrated CNN, transfer learning, and BN with thermography for breast cancer detection,” *Applied Sciences*, vol. 13, no. 1, p. 600, 2023.
8. H. Rahman, T. F. N. Bukht, R. Ahmad, A. Almadhor, and A. R. Javed, “Efficient breast cancer diagnosis from complex mammographic images using deep convolutional neural network,” *Computational Intelligence and Neuroscience*, vol. 2023, no. 1, p. 7717712, 2023.
9. J. J. Y. Huang, K. S. K. Ma, L. T. Wang, C. H. Chiang, S. F. Yang, C. H. Wang, and P. H. Wang, “The risk of endometrial cancer and uterine sarcoma following endometriosis or pelvic inflammatory disease,” *Cancers*, vol. 15, no. 3, p. 833, 2023.
10. Z. Ji, D. Yao, R. Chen, T. Lyu, Q. Liao, L. Zhao, and I. Ganchev, “U-Net_dc: A novel U-Net-based model for endometrial cancer cell image segmentation,” *Information*, vol. 14, no. 7, p. 366, 2023.
11. M. Stukan, P. Rutkowski, J. Smadja, and S. Bonvalot, “Ultrasound-guided trans-uterine cavity core needle biopsy of uterine myometrial tumors to differentiate sarcoma from a benign lesion—description of the method and review of the literature,” *Diagnostics*, vol. 12, no. 6, p. 1348, 2022.

12. Q. Li, R. Wang, Z. Xie, L. Zhao, Y. Wang, C. Sun, L. Han, Y. Liu, H. Hou, C. Liu, G. Zhang, G. Shi, D. Zhong, and Q. Li, “Clinically applicable pathological diagnosis system for cell clumps in endometrial cancer screening via deep convolutional neural networks,” *Cancers*, vol. 14, no. 17, p. 4109, 2022.
13. D. Zhao, Z. Zhang, Z. Wang, Z. Du, M. Wu, T. Zhang, J. Zhou, W. Zhao, and Y. Meng, “Diagnosis and prediction of endometrial carcinoma using machine learning and artificial neural networks based on public databases,” *Genes*, vol. 13, no. 6, p. 935, 2022.
14. D. Jiménez-Sánchez, Á. López-Janeiro, M. Villalba-Esparza, M. Ariz, E. Kadioglu, I. Masetto, V. Goubert, M. D. Lozano, I. Melero, D. Hardisson, C. Ortiz-De-Solórzano, and C. E. De Andrea, “Weakly supervised deep learning to predict recurrence in low-grade endometrial cancer from multiplexed immunofluorescence images,” *NPJ Digital Medicine*, vol. 6, no. 1, p. 48, 2023.
15. M. Toğaçar, “Detection of segmented uterine cancer images by Hotspot Detection method using deep learning models, Pigeon-Inspired Optimization, types-based dominant activation selection approaches,” *Computers in Biology and Medicine*, vol. 136, no. 9, p. 104659, 2021.
16. M. G. Hemeida, A. A. Ibrahim, A. A. A. Mohamed, S. Alkhalaf, and A. M. B. El-Dine, “Optimal allocation of distributed generators DG based Manta Ray Foraging Optimization algorithm (MRFO),” *Ain Shams Engineering Journal*, vol. 12, no. 1, pp. 609–619, 2021.